IEEE Access
Multidisciplinary | Rapid Review | Open Access Journal

Received August 7, 2018, accepted September 22, 2018, date of publication October 4, 2018, date of current version October 29, 2018.

Digital Object Identifier 10.1109/ACCESS.2018.2873571

Ultra-Wideband Based Pose Estimation for Small Unmanned Aerial Vehicles

MICHAEL STROHMEIER, THOMAS WALTER, JULIAN ROTHE, AND SERGIO MONTENEGRO
Department of Aerospace Information Technology, University of Würzburg, 97074 Würzburg, Germany

Corresponding author: Michael Strohmeier (michael.strohmeier@uni-wuerzburg.de)

This work was supported in part by the German Federal Ministry for Economic Affairs and Energy, in part by the German Research Foundation, and in part by the University of Würzburg through the Open Access Publish Funding Programme.

ABSTRACT This paper proposes a 3-D local pose estimation system for a small Unmanned Aerial Vehicle (UAV) with a weight limit of 200 g and a very small footprint of 10 cm × 10 cm. The system is realized by fusing 3-D position estimations from an Ultra-Wide Band (UWB) transceiver network with Inertial Measurement Unit (IMU) sensor data and data from a barometric pressure sensor. The 3-D position from the UWB network is estimated using Multi-Dimensional Scaling (MDS) and range measurements between the transceivers. The range measurements are obtained using Double-Sided Two-Way Ranging (DS-TWR), thus eliminating the need for an additional clock synchronization mechanism. The sensor fusion is accomplished using a loosely coupled Extended Kalman Filter (EKF) architecture. Extensive evaluation of the proposed system shows that a position accuracy with a Root-Mean-Square Error (RMSE) of 0.20 *cm* can be obtained. The orientation angle can be estimated with an RMSE of 1.93°.

INDEX TERMS DecaWave, extended Kalman filter, pose estimation, UAV, UWB.

I. INTRODUCTION

The DLR Space Agency's Valles Marineris Exploration (VaMEx) mission aims to explore the Valles Marineris on planet Mars, an area that is poorly investigated due to the challenging topology in this region with deep canyons and high mountains. The mission concept foresees the use of an autonomous swarm of agents with different types of locomotion. Multiple Unmanned Aerial Vehicles (UAVs) as well as Unmanned Ground Vehicles (UGVs) will be deployed from a lander system [1]. All swarm members act in a cooperative way, i.e. some members explore the terrain informing the other members about the location of interesting features.

Within VaMEx, the Local Ad-hoc Positioning and Landing System (LAOLa) project focuses on the development of a reliable navigation concept for a later mission on Mars [2]. Due to the conceptional character of this project, its focus is rather on the development of suitable algorithms than on the deployment of radiation hardened and space proofed hardware. One goal of LAOLa is to implement reliable communication and a Local Positioning System (LPS) between all agents and the lander. Furthermore, the lander should be able to estimate a global position, thus allowing to reference all agents globally, too.

A. RELATED WORK

Although, LPS methods based on Ultra-Wide Band (UWB) technology are well researched and commercial solutions are already available, use case scenarios are mostly targeted towards warehouse and industrial applications [3]–[7]. Those applications assume approximately static but cluttered environments where additional a priori known information, such as existing maps as well as the exact position of the so called UWB anchors are available. Infrastructure that allows a reliable communication between the anchors without occupying additional bandwidth exists usually. Another major branch of UWB based navigation research focuses on the seamless transition between and the combination of different navigation systems. The investigated scenarios typically focus on multi path prone and GNSS denied environments where UWB measurements are combined with GNSS observations and navigation data from other systems, such as optical and intertial navigation systems [8]–[11]. With the availability of cost efficient and miniaturized UWB transceivers, in recent years, the research focus shifted towards the integration of UWB transceivers for navigation purposes on small UAVs.

Especially on small UAVs, the high vehicle dynamics, the very limited computational power and the hard real-time

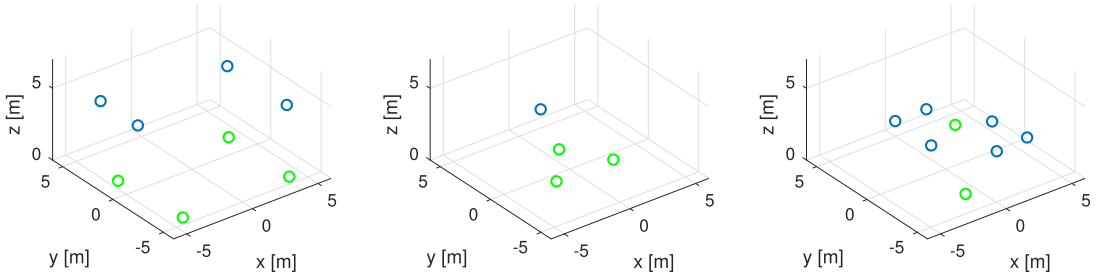

FIGURE 1. Different anchor configurations for UWB localization: Tiemann et al. [12] (right), Ledergerber et al. [13] (left), and in this paper (middle). Anchors with a similar height have the same color.

constraints as well as the required accuracy demands are challenging.

Tiemann and Wietfeld [12] describe a LPS for a scalable multi agent UAV system in a warehouse scenario. For each agent-anchor pair Time Difference of Arrival (TDOA) measurements are obtained and fused in an Extended Kalman Filter (EKF). In order to obtain valid TDOA measurements the UWB anchors are wirelessly synchronized [14]. In their research, the fixed anchors operate as receivers, whereas the UAVs initiate the TDOA range measurements. The UAV's relative orientation between the LPS-coordinate frame and the UAV body frame is obtained using an external optical tracking system. In the setup proposed in [12] eight anchors are used for the localization while an additional anchor is needed for time synchronization. The implemented system is based on a Parrot Bebop, running the low-level UAV control and Linux. A dedicated micro processor for collecting UWB range measurements was used.

A similar approach was chosen by Ledergerber *et al.* [13]. However, in their work the fixed anchors initiate Time of Arrival (TOA) measurements sequentially, while the UAV acts as receiver. The advantage of their approach is a higher scalability since the system performance depends on the number of anchors rather than on the number of UAVs. Both, a TDOA and a TOA approach are investigated. Additionally to the UAV position and attitude, the rotation between the initial and the body frame is estimated in an EKF. The EKF was originally proposed in a previous publication by Mueller *et al.* [15] but utilized Two-Way Ranging with Multiple Acknowledgements (TWR-MA) measurements instead. Again, eight anchors were used for localization. The system is based on the Asctec Hummingbird, a commercial drone with a dedicated low-level flight processor and a high level processor running Linux. The Hummingbird was additionally equipped with a Pixhawk Flight Controller for UWB pose estimation.

This paper focuses on a small footprint UAV's pose estimation based on UWB Components-Off-The-Shelf (COTS) transceivers. On this small UAV only a single embedded processor is used for attitude estimation, UWB pose estimation, UAV flight control and data logging. While a higher number and a uniform distribution of anchors decrease the position inaccuracy of an UWB based navigation system, the communication effort increases drastically. With only four UWB anchors, a minimal configuration of anchors will be used that allows a valid 3D position estimation with low communication load. A comparison of different anchor configurations in typical test scenarios is given in Figure 1.

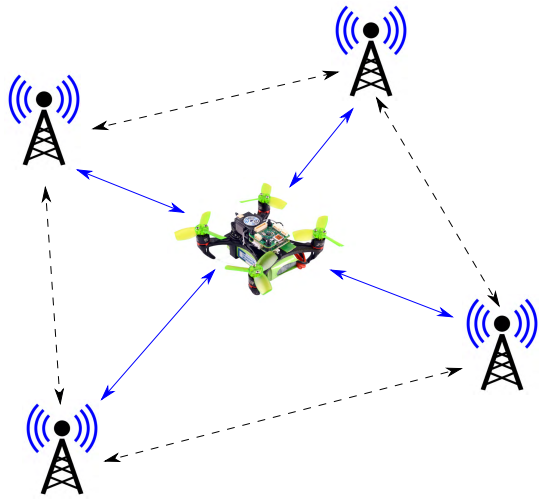

FIGURE 2. UAV pose estimation based on DS-TWR. After the configuration of the fixed anchors is obtained (dotted lines), only the position of the UAV is estimated (blue lines).

The anchor constellation as well as the UAV position are estimated using Double-Sided Two-Way Ranging (DS-TWR) and Multi-Dimensional Scaling (MDS). In a loosely-coupled EKF, the UAV position, accelerometer, gyroscope and magnetometer data from the IMU as well as barometer measurements are combined. In a future Mars scenario, the magnetic heading has to be replaced by another reference system since there is no global magnetic field available for navigation on Mars. Since the exact position of the anchors is initially not known within the LAOLa scenario, the full UWB node constellation will be initially estimated using DS-TWR, however, during the UAV flight, only the signal propagation times between the UAV and the anchors are measured using DS-TWR (see Figure 2).

II. SYSTEM ARCHITECTURE

The proposed system is based on a non-commercial UAV with a footprint of $10\,cm \times 10\,cm$ and a weight of less than 200g which was developed at the University of Würzburg.

Inter-board connectors routing various interfaces of the main processor allow to easily add different sensors and interfaces, such as WiFi, GPS or a SD-Card. The UAV's autopilot runs on board a cortex M4 processor using the Real-time Onboard Dependable Operating System (RODOS) [16]. The configuration shown in Figure 3 includes the following components:

- Micro-processor (*STMicroelectronics: STM32F407VG*)
- Accelerometer, Gyroscope, Magnetometer (*STMicroelectronics: LSM9DS1*)
- Barometer (*Measurement Specialties: MS5611*)
- UWB transceiver (*DecaWave: DWM1000*)
- Remote receiver (*Spektrum: DSMX*)
- Electronic speed controller (*Sunrise: Cicada-30A-4in1*)

FIGURE 3. UAV platform used in this work.

A. COORDINATE SYSTEMS

Figure 4 gives an overview of coordinate frames that are relevant for this work. The body frame is fixed to the UAV and its x^b-axis is aligned to the UAV longitudinal axis, its z^b-axis is perpendicular to the UAV center plate and intersects with the UAV's center of gravity. Its y^b-axis is chosen to be right-handed orthogonal.

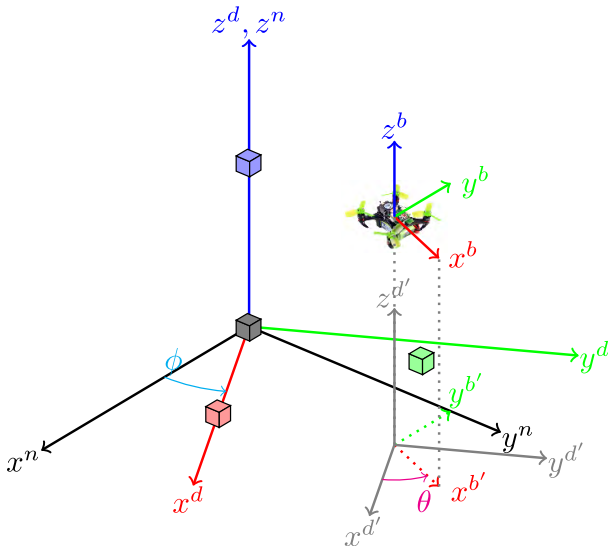

FIGURE 4. Important coordinate frames for this work: DecaWave frame (*d*), Navigation frame (*n*), the body frame (*b*), the translated DecaWave frame (*d'*) and the projected body frame (*b'*). A possible UWB anchor configuration is shown: ID0 (grey), ID1 (red), ID2 (green), ID3(blue).

The origin of the navigation frame is the position of the ID0 UWB anchor. Its x^n-axis is pointing towards magnetic north, and its z^n-axis in the opposite direction of the Earth's gravitational force. The y^n-axis is again right-handed orthogonal.

The DecaWave frame is constructed based on the position of the UWB anchors. For simplicity it is assumed that the anchors ID0, ID1 and ID2 are in the same height on a plane ground and approximately construct a right-handed coordinate frame while the anchor ID3 is above that plane. Based on those assumptions, the x^d-axis is defined by the ID0-ID1 anchor line of sight and the $x^d y^d$-plane is defined using anchor ID2 and the direction of the z^d-axis using anchor ID3.

Consequently, the origin and the z-axis of the DecaWave frame and the navigation frame are identical. However, the two frames are rotated against each other about a fixed but unknown angle ϕ. Since the UAV's position control relies on measurements in the body frame, position estimates in the DecaWave frame have to be rotated into the body frame. In this approach we do not attempt to estimate ϕ directly, but rather the rotation angle θ between the projection of the x^b-axis onto the $x^n y^n$-plane of the navigation frame and the virtual $x^{d'}$-axis using an Extended Kalman Filter. The axes of the translated DecaWave frame are parallel to the axes of the DecaWave frame, but the origin is the projection of the UAV's center of gravity onto the $x^n y^n$-plane.

The approach proposed in this work is summarized in Figure 5. Measurements of the accelerometer $\boldsymbol{y}_a^b$, the gyroscope $\boldsymbol{y}_g^b$ and the magnetometer $\boldsymbol{y}_m^b$ are combined to estimate the UAV's attitude using the approach described in [17]. Additionally to the attitude quaternion $\boldsymbol{q}^{nb}$, the bias-free rotational velocity of the UAV $\boldsymbol{\omega}^b$ is also estimated. The output of the Attitude Heading Reference System (AHRS) as well as the low-pass filtered accelerometer raw measurements $\hat{\boldsymbol{y}}_a^b$ are used to propagate the pose estimation EKF. Using the UWB network, distance measurements d_i between the relevant nodes are collected. Using MDS, the constellation of the UWB network is calculated and therefore the position of the UAV relative to the UWB anchors is known. Both, the UAV position $\boldsymbol{y}_{UWB}^d$ and the barometric height information $\boldsymbol{y}_{baro}$ are used in the EKF update steps.

B. DOUBLE-SIDED TWO-WAY RANGING

The distances between UAV-anchor pairs and anchor-anchor pairs are obtained using Double-Sided Two-Way Ranging as described in DecaWave's application note [18]. The main advantage of DS-TWR is to measure the time of flight t_{oF} between two UWB instances without the need for an additional clock synchronization. However, compared to other methods, such as TOA or TDOA based approaches, more communication between the UWB nodes is required leading to a higher bandwidth utilization which decreases the

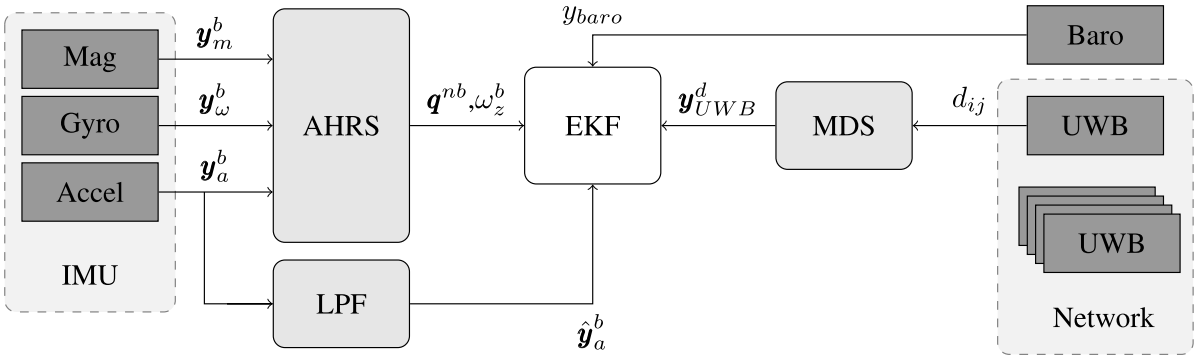

FIGURE 5. Proposed UWB localization system architecture.

measurement rate. Nevertheless, with four anchors and a single UAV, a maximum rate of about 5 Hz was achieved, which is comparable to the update rate of low cost GNSS receivers that are commonly used in commercial UAVs.

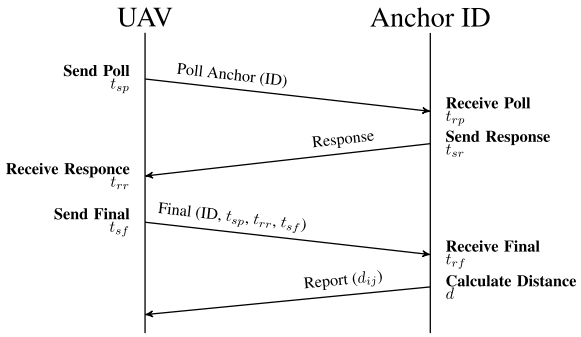

FIGURE 6. Timestamps and communication required for a single UAV-anchor pair using DS-TWR.

Figure 6 summarizes the communication flow for a single UAV-anchor pair. The DS-TWR is initiated by a poll message sent from the UAV addressing an anchor with a certain ID. The transmitting time t_{sp} and the receiving time t_{rp} are logged before the anchor with the correct ID responses to the poll message. Again, the transmitting time of the response t_{sr} as well as the receiving time of the response t_{rr} are logged on the anchor and the UAV, respectively. The distance measurement is finalized with a third message reporting the times measured by the UAV to the anchor. The third message includes its own transmission time stamp t_{sf}. Using the time measurements received from the UAV, the previously recorded timestamps as well as the receiving time of the final message t_{rf} the time of flight for a message between both nodes can be computed by:

$$t_{oF} = \frac{\left(t_{rr} - t_{sp}\right)\left(t_{sr} - t_{rr}\right) - \left(t_{sr} - t_{rp}\right)\left(t_{rf} - t_{sr}\right)}{t_{sf} - t_{sp} + t_{rf} - t_{rp}} \quad (1)$$

Using the speed of light in air, the distance between both nodes can be easily calculated with:

$$d = t_{oF} \cdot c_{air} \quad (2)$$

Once the distance between a node pair is calculated, the result is reported back to the UAV, resulting in a total number of four messages per distance measurement. In addition to those four messages, mechanisms to coordinate the channel utilization and the communication between all nodes are required. In the proposed approach, the UAV itself acts as master, initiating distance measurements to the other anchors sequentially. Before take-off, the distance measurements collected for the fixed anchors are averaged. Once the UAV is air born, only the distances between the UAV and the fixed anchors are measured.

C. MULTI-DIMENSIONAL SCALING

Using Multi-Dimensional Scaling, particularly classical scaling, which was first introduced by Torgerson [19], and the distance measurements d_{ij} obtained with DS-TWR, the full UWB node configuration can be estimated. In our approach, the algorithm determines a set of 3-dimensional points $x_1, ..., x_N \in \mathbb{R}^3$ for each UWB node with ID $i = 1, ..., N$, in such a way that the difference between the observed distances d_{ij} and the computed distance $\|x_i - x_j\|$ is minimized. In order to determine the best fitting set, the loss function in Equation 3 was introduced by Kruskal [20]:

$$loss_d(x_1, ..., x_N) = \sqrt{\sum_{i=1, i\neq j}^{N} \left(d_{ij} - \|x_i - x_j\|\right)^2} \quad (3)$$

The loss function can be efficiently minimized using a gradient descent approach, iteratively moving the 3D point estimates $x_1, ..., x_N$ until a suitable set is found. Since the points of the solution are not referenced to the DecaWave frame, the estimated constellation is transformed according to the setup of the DecaWave frame described in Section II.

D. EXTENDED KALMAN FILTER

The position estimate obtained from the MDS algorithm, inertial navigation data measured on the UAV and the UAV's barometric altitude are combined in an Extended Kalman Filter in order to estimate the UAV's position and velocity in the DecaWave frame. Furthermore, the rotation angle θ

between the UAV fixed body frame and the DecaWave frame is estimated.

1) MEASUREMENT MODELS

The MDS UAV position estimate is assumed to have Additivie White Gaussian Noise (AWGN) only. The position measurement model $\boldsymbol{y}^d_{UWB}$ is therefore the sum of the actual position $\boldsymbol{p}^d$ and additive noise $\boldsymbol{v}_{UWB}$ with a variance $\sigma_{UWB}{}^2$:

$$\boldsymbol{y}^d_{UWB} = \boldsymbol{p}^d + \boldsymbol{v}_{UWB} \tag{4}$$

The IMU provides 3-dimensional gyroscope and accelerometer measurements in the UAV's body frame. The gyroscope measurement $\boldsymbol{y}^b_g$ can be modeled by:

$$\boldsymbol{y}^b_g = \boldsymbol{\omega}^b + \boldsymbol{b}_g + \boldsymbol{v}_g \tag{5}$$

where $\boldsymbol{\omega}^b$ is the angular rate in the body frame, $\boldsymbol{b}_g$ is the temperature depended gyro bias and $\boldsymbol{v}_g$ is AWGN with a variance of $\sigma_g{}^2$.

The low-pass filtered accelerometer measurement $\hat{\boldsymbol{y}}^b_a$ is modeled as:

$$\hat{\boldsymbol{y}}^b_a = \boldsymbol{a}^b - \boldsymbol{g}^b + \boldsymbol{b}_a + \boldsymbol{v}_a \tag{6}$$

where $\boldsymbol{a}^b$ is the acceleration acting on the UAV, $\boldsymbol{g}^b$ is the Earth's gravity vector expressed in the body frame, $\boldsymbol{b}_a$ is the accelerometer bias and $\boldsymbol{v}_a$ is AWGN with a variance of $\sigma_a{}^2$.

Finally, the barometric altitude measurement y_{baro} can be modeled as:

$$y_{baro} = \rho_{baro} + \Delta z + \upsilon_{baro} \tag{7}$$

where ρ_{baro} is the height of the UAV, Δz is the known altitude offset between the DecaWave frame and barometric height and υ_{baro} is AWGN with a variance of $\sigma_{baro}{}^2$.

2) SYSTEM PROPAGATION MODEL

Additionally to the position $\boldsymbol{p}^d$, the velocity $\boldsymbol{v}^d$ and the rotation angle θ, the accelerometer bias should be estimated. In order to reduce the EKF complexity we do not estimate the accelerometer bias in the body frame but rather in the projected body frame $\boldsymbol{b}^{b'}_a$ where the $z^{b'}$-axis is aligned with the Earth's gravity vector. The full EKF system state $\hat{\boldsymbol{x}}(k|k)$ at the time k is therefore given by:

$$\hat{\boldsymbol{x}}(k|k) = \left[\boldsymbol{p}^d(k|k)^T \ \boldsymbol{v}^d(k|k)^T \ \theta(k|k) \ \boldsymbol{b}^{b'}_a(k|k)^T\right]^T \tag{8}$$

The system state is propagated at a fixed rate which corresponds to the sampling time Δt of the IMU. The system propagation is modeled by a non-linear function that depends on the previously known state, the accelerometer measurement in the projected body frame $\boldsymbol{y}^{b'}_a$ and the rotational velocity around the $z^{b'}$-axis $\omega^{b'}_z$:

$$\hat{\boldsymbol{x}}(k+1|k) = f\left(k, \Delta t, \hat{\boldsymbol{x}}(k|k), \hat{\boldsymbol{y}}^{b'}_a(k), \omega^{b'}_z(k)\right) \tag{9}$$

In Equation 9, $\boldsymbol{y}^{b'}_a$ and $\omega^{b'}_z$ are obtained by utilizing the attitude quaternion $\boldsymbol{q}^{nb}$ and the bias-free rotational velocity $\boldsymbol{\omega}^b$ that were previously estimated using the AHRS as depicted in Figure 5. The two required EKF inputs are calculated by rotating the raw measurement $\boldsymbol{y}^b_a$ and the bias-free rotational velocity $\boldsymbol{\omega}^b$ around the roll and pitch angle that are encoded in the quaternion $\boldsymbol{q}^{nb}$.

In detail, the complete system propagation is given by the following set of equations:

$$\begin{aligned}\boldsymbol{p}^d(k+1|k) &= \boldsymbol{p}^d(k|k) + \Delta t \cdot \boldsymbol{v}^d(k|k) \\ &\quad + \frac{1}{2}\Delta t^2 \boldsymbol{R}_z(\theta(k|k)) \cdot (\hat{\boldsymbol{y}}^{b'}_a(k) - \boldsymbol{b}^{b'}_a(k|k)) \end{aligned} \tag{10}$$

$$\begin{aligned}\boldsymbol{v}^d(k+1|k) &= \boldsymbol{v}^d(k|k) \\ &\quad + \Delta t \boldsymbol{R}_z(\theta(k|k)) \cdot (\hat{\boldsymbol{y}}^{b'}_a(k) - \boldsymbol{b}^{b'}_a(k|k)) \end{aligned} \tag{11}$$

$$\theta(k+1|k) = \theta(k|k) + \Delta t \cdot \omega^{b'}_z(k) \tag{12}$$

$$\boldsymbol{b}^{b'}_a(k+1|k) = \boldsymbol{b}^{b'}_a(k|k) \tag{13}$$

where $\boldsymbol{R}_z(\theta)$ is simply the rotation matrix around the z-axis for a given angle θ:

$$\boldsymbol{R}_z(\theta) = \begin{bmatrix} \cos\theta & -\sin\theta & 0 \\ \sin\theta & \cos\theta & 0 \\ 0 & 0 & 1 \end{bmatrix} \tag{14}$$

The system state covariance matrix P is propagated using the following equation:

$$\begin{aligned}\boldsymbol{P}(k+1|k) &= \nabla \boldsymbol{F}_x(k) \boldsymbol{P}(k|k) \nabla \boldsymbol{F}_x(k)^T \\ &\quad + \nabla \boldsymbol{F}_u(k) \boldsymbol{U} \nabla \boldsymbol{F}_u(k)^T \end{aligned} \tag{15}$$

where $\nabla \boldsymbol{F}_x$ and $\nabla \boldsymbol{F}_u$ are the Jacobians of the system prediction function f with respect to the system state $\hat{\boldsymbol{x}}(k|k)$ and the system input $\boldsymbol{u}$, respectively.

The Jacobians of the system prediction function are therefore:

$$\nabla \boldsymbol{F}_x(k) = \left.\frac{\partial f(k)}{\partial \boldsymbol{x}}\right|_{\boldsymbol{x}=\hat{\boldsymbol{x}}(k|k)} \tag{16}$$

$$\nabla \boldsymbol{F}_u(k) = \left.\frac{\partial f(k)}{\partial \boldsymbol{u}}\right|_{\boldsymbol{u}=\left[\boldsymbol{y}^{b'}_a(k) \ \omega^{b'}_z(k)\right]^T} \tag{17}$$

The noise matrix $\boldsymbol{U}$ is given by:

$$\boldsymbol{U} = \begin{bmatrix} \sigma_a^2 & 0 & 0 \\ 0 & \sigma_a^2 & 0 \\ 0 & 0 & \sigma_g^2 \end{bmatrix} \tag{18}$$

3) MEASUREMENT UPDATES

Measurement updates can occur at different times and are integrated into the EKF at their respective rates, i.e. a new position measurement $\boldsymbol{y}^d_p$ is received every 200 ms and the barometric height y_{baro} is measured every 30 ms. The measurement update for the system state and the system state covariance are given by the following equations:

$$\begin{aligned}\hat{\boldsymbol{x}}(k+1|k+1) &= \hat{\boldsymbol{x}}(k+1|k) + \boldsymbol{W}(k+1) \\ &\quad \cdot \left(\boldsymbol{z}_i(k+1) - \hat{\boldsymbol{z}}_i(k+1|k)\right) \end{aligned} \tag{19}$$

$$\begin{aligned}\boldsymbol{P}(k+1|k+1) &= \boldsymbol{P}(k+1|k) \\ &\quad + \boldsymbol{W}(k+1) \boldsymbol{S}_i(k+1) \boldsymbol{W}(k+1)^T \end{aligned} \tag{20}$$

where z_i is the latest measurement and $\hat{z}_i$ is the current measurement prediction. $\boldsymbol{W}$ is the Kalman Filter gain and $\boldsymbol{S}_i$ is the residual covariance matrix. Depending on the sensor source, we can select $i \in \{UWB, baro\}$. The Kalman Filter gain and the residual covariance are given by:

$$\boldsymbol{S}_i(k+1) = \boldsymbol{H}_i(k+1)\boldsymbol{P}(k+1|k)\boldsymbol{H}_i(k+1)^T + \boldsymbol{R}_i \quad (21)$$

$$\boldsymbol{W}(k+1) = \boldsymbol{P}(k+1|k)\boldsymbol{H}_i(k+1)^T\boldsymbol{S}_i(k+1)^{-1} \quad (22)$$

where $\boldsymbol{H}_i$ is the matrix that predicts the next measurement based on the current state estimation and $\boldsymbol{R}_i$ is the respective sensor noise term.

The measurement prediction matrices $\boldsymbol{H}_{UWB}$ and $\boldsymbol{H}_{baro}$ are simply:

$$\boldsymbol{H}_{UWB} = \begin{bmatrix} 1 & 0 & 0 & 0 & 0 & 0 & 0 & 0 & 0 & 0 \\ 0 & 1 & 0 & 0 & 0 & 0 & 0 & 0 & 0 & 0 \\ 0 & 0 & 1 & 0 & 0 & 0 & 0 & 0 & 0 & 0 \end{bmatrix} \quad (23)$$

$$\boldsymbol{H}_{baro} = \begin{bmatrix} 0 & 0 & 1 & 0 & 0 & 0 & 0 & 0 & 0 & 0 \end{bmatrix} \quad (24)$$

The measurements and the corresponding noise matrices are given by:

$$z_{UWB} = \boldsymbol{y}^d_{UWB}, \quad \boldsymbol{R}_{UWB} = diag\left(\sigma^2_{UWB}\right) \quad (25)$$

$$z_{baro} = y_{baro} - \Delta z, \quad \boldsymbol{R}_{baro} = \sigma^2_{baro} \quad (26)$$

4) EKF INITIALIZATION

In order to detect whether θ is estimated correctly, multiple instances of the proposed EKF run simultaneously. While the same measurements are used, the filters are initialized with different start values for θ. Additionally, the assumed gyroscope noise in the system propagation noise covariance matrix $\boldsymbol{U}$ is increased, in order to allow the EKF instances to converge faster. Once all filters converged within a certain threshold towards a common value, the assumed gyroscope noise is decreased to its original value again and only a single EKF instance continues to run. Figure 7 shows the estimated θ_i from three different EKF instances during an ideal circular calibration maneuver. The convergence criteria for N EKF instances and a threshold of δ_{Th} is:

$$\sum_{i=1}^{N}\left(\theta_i - \sum_{j=1}^{N}\frac{\theta_j}{N}\right) < \delta_{Th} \quad (27)$$

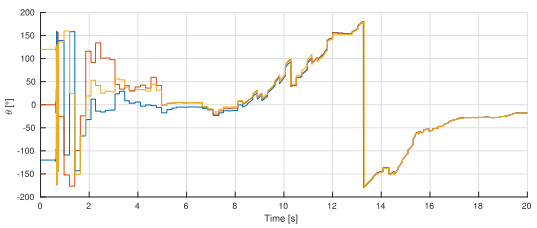

FIGURE 7. θ estimates from a simulation for the three EKF instances. The three initial estimates are at $\{-120°, 0°, 120°\}$ and converge within 20 *s*.

III. RESULTS

The proposed system was implemented on a single processor. Using the IMU data, the EKF was propagated at 200 Hz, while the DecaWave position and the barometric height measurement updates were integrated at their sampling rates of 5 Hz and 30 Hz, respectively. Both experiments presented in this section were conducted in the indoor flight cage of the University of Würzburg as shown in Figure 8.

For reference, the UAV's true position was determined using the OptiTrack Flex 3 optical tracking system and its data was logged using an external ground station while the EKF states were logged using a SD card extension on the UAV. Both systems, the UAV and the ground station, were time synchronized. In order to evaluate the proposed system, two different scenarios were investigated. First, the quality of the UAV's rotation angle θ estimation is analyzed. Therefore, after a random, manual calibration flight for EKF convergence, the UAV is commanded to hold its position while the EKF states are logged utilizing the DecaWave position estimates as position control-loop feedback. The second experiment examines the UAV's position accuracy. In this setup no initial calibration flight is performed but the UAV is commanded to follow a specific path with a fixed orientation using optical tracking data as reference instead.

A. ROTATION ANGLE ESTIMATION

This experiment can be divided into two stages. During the first stage, the UAV is commanded manually to allow the three simultaneously running EKF instances to converge. In the second stage, which begins shortly after the θ estimates converged, the UAV is commanded to hold its position using the EKF position and velocity estimate. The results of this experiment are outlined in Figure 9.

Flying a random pattern, the three EKF instances take almost 65 s to converge. Once a valid θ estimate is found, the error between the EKF estimate θ and angle measured with the optical tracking reference system remains within a 3.5° error band with a RMSE of 1.93°. The θ error quantiles are compared for the first stage, the second stage and the complete experiment in Table 1. Table 2 outlines the position error quantiles during the first stage, while Table 3 gives the error quantiles during the second stage. The horizontal RMSE during the second stage is found to be 0.12 *cm* and the 3D position RMSE is 0.19 *cm*.

TABLE 1. θ Error quantiles.

	Q(50%) [°]	Q(75%) [°]	Q(90%) [°]	Q(95%) [°]	Q(99%) [°]
1st	13.65	22.05	30.38	69.70	147.99
2nd	1.77	2.40	3.10	3.24	3.49
all	2.34	5.08	20.83	25.57	122.52

Comparing both tables, it can be clearly seen that the error quantiles during the second stage are smaller than during the manual calibration flight. There are two reasons for this observation. First, the estimated θ angle is more accurate and

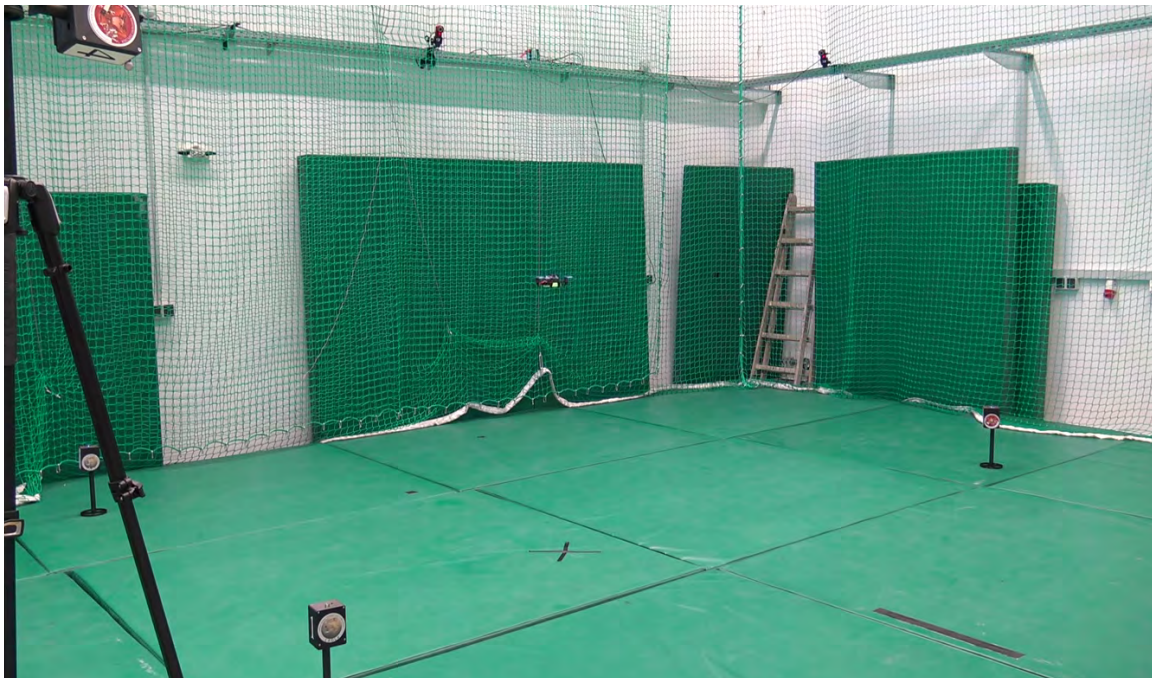

FIGURE 8. Indoor flight cage at the University of Würzburg.

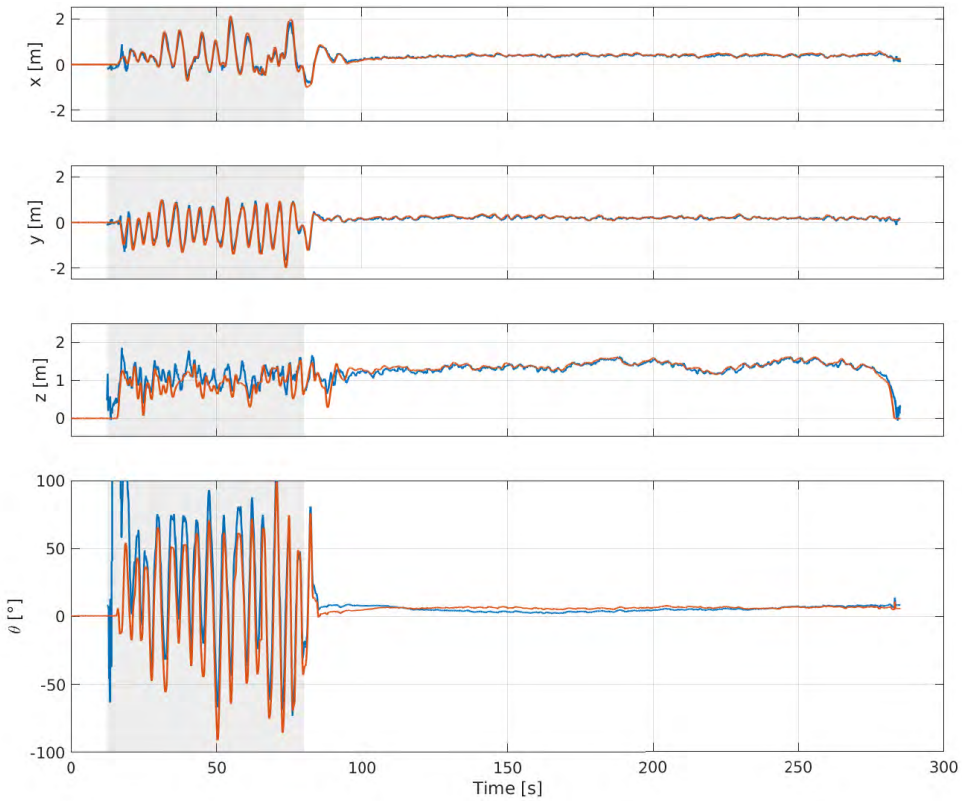

FIGURE 9. Position p^d and rotation angle θ estimated using the proposed EKF (blue) compared to the optical tracking reference (red). The time needed for the filter to converge is indicated using a gray background and ends approximately 65 s after take off.

therefore the system state propagation equations 10 and 11 are a more reliable estimation of the true system propagation. Second, the position accuracy of the UWB MDS algorithm depends heavily on the system dynamics, since MDS assumes that the distances are obtained simultaneously. However, the measurements are obtained sequentially and each of the

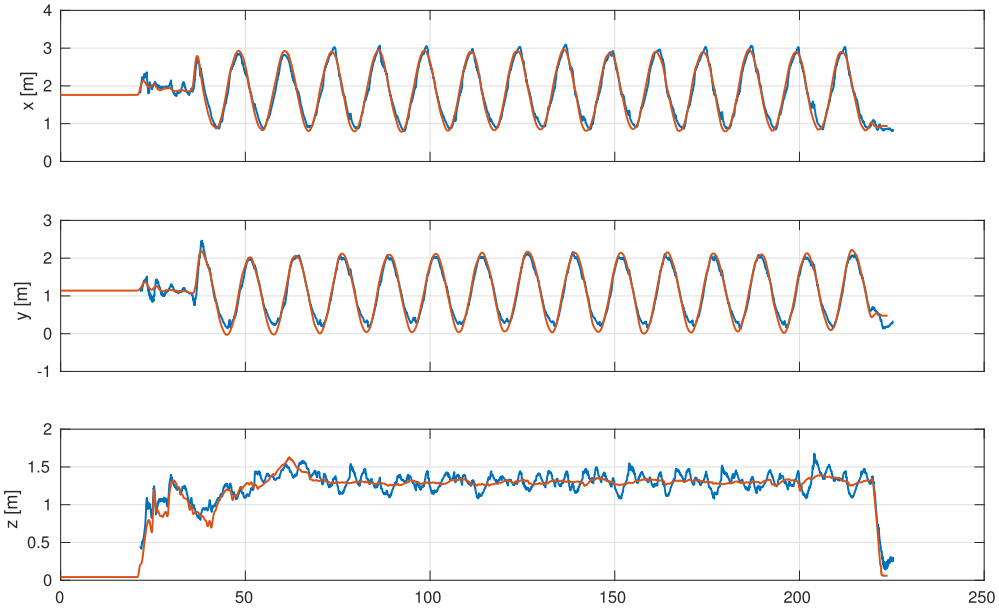

FIGURE 10. Each axis plot individually during the second experiment: The optical reference system (red) and the EKF position estimate (blue). A systematic error can be observed for each axis.

TABLE 2. Error quantiles during the first stage of the first experiment.

	Q(50%) [m]	Q(75%) [m]	Q(90%) [m]	Q(95%) [m]	Q(99%) [m]
x	0.080	0.138	0.204	0.269	0.398
y	0.090	0.163	0.222	0.255	0.391
z	0.151	0.282	0.373	0.422	0.536
2D	0.145	0.215	0.281	0.334	0.499
3D	0.256	0.348	0.444	0.508	0.622

TABLE 3. Error quantiles during the second stage of the first experiment.

	Q(50%) [m]	Q(75%) [m]	Q(90%) [m]	Q(95%) [m]	Q(99%) [m]
x	0.024	0.039	0.055	0.067	0.090
y	0.022	0.04	0.061	0.073	0.102
z	0.062	0.087	0.112	0.135	0.225
2D	0.039	0.056	0.076	0.09	0.118
3D	0.079	0.101	0.128	0.15	0.254

measurements is error afflicted due to the movement of the UAV. Consequently, there is a systematic error in the MDS position estimation, which increases with the system dynamics. During position hold, the UAV is able to remain within a 3σ bound of 0.15 cm in x and y direction and 0.30 cm in z direction.

B. REAL-TIME LOCATION SYSTEM ACCURACY

In the second experiment we evaluate complete proposed Real-time Location System accuracy with higher system dynamics. Therefore, the UAV is commanded to fly on a predefined circular trajectory with 1 m/s utilizing the optical tracking system as trajectory reference for the UAV control.

The optical tracking position measurements are transferred to the UAV wirelessly in real-time using a second UWB module whereby, in order to avoid UWB cross talk, one UWB channel is applied for communication and another one for the distance measurements.

The error quantiles for this second setup are outlined in Table 4. The mean horizontal position RMSE is found to be 0.18 m while the RMSE for the mean 3D position is slightly higher with 0.20 m.

TABLE 4. Error quantiles during the second experiment.

	Q(50%) [m]	Q(75%) [m]	Q(90%) [m]	Q(95%) [m]	Q(99%) [m]
x	0.096	0.154	0.207	0.235	0.289
y	0.091	0.152	0.226	0.251	0.297
z	0.066	0.111	0.161	0.184	0.220
2D	0.158	0.213	0.277	0.31	0.362
3D	0.185	0.239	0.297	0.328	0.387

Figure 11 shows the horizontal trajectory of the UAV and the UWB anchor positions. From Figure 11, an error can be observed which most likely correlates to the three anchors that are in the same height and the orientation of the UAV UWB antenna. During the transition form one anchor to another, the position estimate differs from the reference trajectory, while they are in close agreement once the UAV is close to one of the anchors.

The systematics of this error can also be observed if each axis is plotted individually as in Figure 10. The most likely explanation is the antenna orientation on board the UAV and therefore a non-isotropic antenna radiation pattern which is additionally distorted by the influence of UAV structure. Since the UAV's attitude remained constant during

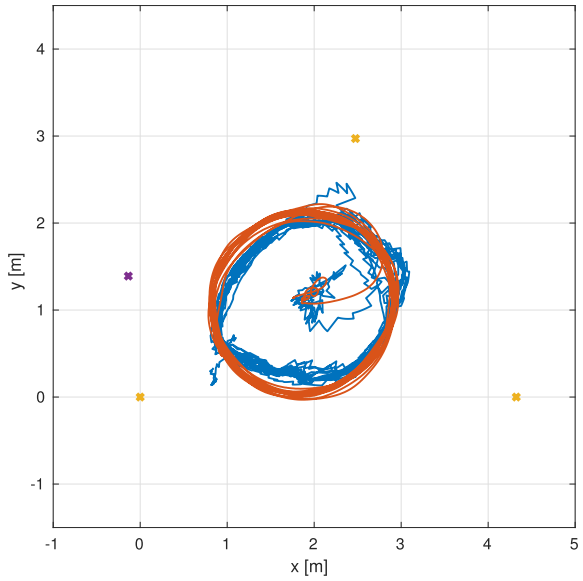

FIGURE 11. 2D trajectory during the second experiment: The optical reference system (red) and the EKF position estimate (blue). Additionally, the anchor positions are indicated (x). The anchors in yellow are at a common height of approximately 0.3 *m*, while the purple anchor is at a height of 4.1 *m*.

this experiment, depending on the UAV position, different anchors have different visibility which causes anchors that are not in a direct line of sight to the antenna to be more error afflicted resulting in degraded distance measurements.

IV. CONCLUSION

This paper presents an approach for a 3D local pose estimation for a small UAV using a single embedded processor for attitude and pose estimation, collecting UWB distance measurements, UAV flight control and data logging at 200 Hz. The proposed approach estimates the UAV position using MDS and additionally the UAV's rotation between the UWB based coordinate frame and the UAV body frame. The range measurements required for MDS are obtained using DS-TWR, thus eliminating the need for an external clock synchronization mechanism. A major drawback of the proposed approach based on DecaWave modules is the increased bandwidth utilization required for a single distance measurement. In terms of scalability, an approach similar to the one described by [13] is definitely favorable.

Additionally, the distance measurements are obtained sequentially while MDS assumes that the distances were obtained simultaneously, resulting in a systematic error that is depended on the vehicle dynamics. However, for low vehicle dynamics, the position can be estimated with a RMSE of 0.19 m while it is slightly higher at 0.20 m considering vehicle dynamics of up to 1 m/s. These observations are consistent with the conclusions drawn by [12] and [13]. Compared to the systematic errors introduced by a non-isotropic radiation pattern, the systematic errors based on the sequential distance measurement are small.

The rotation between the UWB based coordinate frame and the UAV body frame can be reliable estimated with a RMSE of 1.93°. Depending on the calibration flight maneuver, different convergence times for the rotation estimate were achieved. While a detailed classification was not carried out within the scope of this work, circular calibration flights with a continuous change in the UAV's orientation showed to be more effective regarding the convergence time.

REFERENCES

[1] S. Sand *et al.*, "Swarm exploration and navigation on mars," in *Proc. Int. Conf. Localization GNSS (ICL-GNSS)*, Jun. 2013, pp. 1–6.

[2] S. Montenegro, T. Walter, E. Dilger, and M. Becker, "VaMEx—LAOLa—Valles marineris exploration lokales ad-hoc ortungs- und landesystem," in *Proc. 4S Symp.*, 2018, pp. 1–5.

[3] R. J. Fontana, E. Richley, and J. Barney, "Commercialization of an ultra wideband precision asset location system," in *Proc. IEEE Conf. Ultra Wideband Syst. Technol.*, Nov. 2003, pp. 369–373.

[4] Y. Chu and A. Ganz, "A UWB-based 3D location system for indoor environments," in *Proc. 2nd Int. Conf. Broadband Netw. (BroadNets)*, Oct. 2005, pp. 1147–1155.

[5] D. B. Jourdan, D. Dardari, and M. Z. Win, "Position error bound for UWB localization in dense cluttered environments," in *Proc. IEEE Int. Conf. Commun.*, vol. 8, Jun. 2006, pp. 3705–3710.

[6] Y. Zhou, C. Law, Y. Guan, and F. Chin, "Indoor elliptical localization based on asynchronous UWB range measurement," *IEEE Trans. Instrum. Meas.*, vol. 60, no. 1, pp. 248–257, Jan. 2011.

[7] B. Silva, Z. Pang, J. Åkerberg, J. Neander, and G. Hancke, "Experimental study of UWB-based high precision localization for industrial applications," in *Proc. IEEE Int. Conf. Ultra-WideBand (ICUWB)*, Sep. 2014, pp. 280–285.

[8] M. Tanigawa, J. D. Hol, F. Dijkstra, H. Luinge, and P. Slycke, "Augmentation of low-cost GPS/MEMS INS with UWB positioning system for seamless outdoor/indoor positioning," in *Proc. ION GNSS*, Savannah, GA, USA, vol. 4, 2004, pp. 1–8.

[9] J.-A. Fernandez-Madrigal, E. Cruz-Martin, J. Gonzalez, C. Galindo, and J.-L. Blanco, "Application of UWB and GPS technologies for vehicle localization in combined indoor-outdoor environments," in *Proc. ISSPA*, 2007, pp. 1–4.

[10] J. Gonzalez *et al.*, "Combination of UWB and GPS for indoor-outdoor vehicle localization," in *Proc. IEEE Int. Symp. Intell. Signal Process. (WISP)*, Oct. 2007, pp. 1–6.

[11] K. Hausman, S. Weiss, R. Brockers, L. Matthies, and G. S. Sukhatme, "Self-calibrating multi-sensor fusion with probabilistic measurement validation for seamless sensor switching on a UAV," in *Proc. IEEE Int. Conf. Robot. Automat. (ICRA)*, May 2016, pp. 4289–4296.

[12] J. Tiemann and C. Wietfeld, "Scalable and precise multi-UAV indoor navigation using TDOA-based UWB localization," in *Proc. Int. Conf. Indoor Positioning Indoor Navigat. (IPIN)*, Sep. 2017, pp. 1–7.

[13] A. Ledergerber, M. Hamer, and R. D'Andrea, "A robot self-localization system using one-way ultra-wideband communication," in *Proc. IEEE/RSJ Int. Conf. Intell. Robots Syst. (IROS)*, Sep. 2015, pp. 3131–3137.

[14] J. Tiemann, F. Eckermann, and C. Wietfeld, "Multi-user interference and wireless clock synchronization in TDOA-based UWB localization," in *Proc. IPIN*, 2016, pp. 1–6.

[15] M. W. Mueller, M. Hamer, and R. D'Andrea, "Fusing ultra-wideband range measurements with accelerometers and rate gyroscopes for quadrocopter state estimation," in *Proc. IEEE Int. Conf. Robot. Autom. (ICRA)*, May 2015, pp. 1730–1736.

[16] *RODOS—Real-Time Onboard Dependable Operating System*. Accessed: Jan. 15, 2018. [Online]. Available: https://en.wikipedia.org/wiki/Rodos_(operating_system)

[17] M. Strohmeier and S. Montenegro, "Coupled GPS/MEMS IMU attitude determination of small UAVs with COTS," *Electronics*, vol. 6, no. 1, p. 15, 2017.

[18] DecaWave. *APS013: The Implementation of Twoway Ranging With the DW1000*. Accessed: Oct. 7, 2018. [Online]. Available: https://www.decawave.com/wp-content/uploads/2018/08/aps013_dw1000_and_two_way_ranging_v2.2.pdf

[19] W. S. Torgerson, "Multidimensional scaling: I. Theory and method," *Psychometrika*, vol. 17, no. 4, pp. 401–419, Dec. 1952.

[20] J. B. Kruskal, "Multidimensional scaling by optimizing goodness of fit to a nonmetric hypothesis," *Psychometrika*, vol. 29, no. 1, pp. 1–27, Mar. 1964.

MICHAEL STROHMEIER was born in Würzburg, Germany, in 1989. He received the B.S. degree in aerospace computer science from the University of Würzburg, Würzburg, in 2012, and the M.S. degree in space science and technology from Aalto University, Helsinki, Finland, and the Luleå University of Technology, Luleå, Sweden, in 2014. He is currently pursuing the Ph.D. degree with the Department of Aerospace Information Technology, University of Würzburg. From 2010 to 2013, he was a Student Assistant with the Department of Aerospace Information Technology, University of Würzburg, where he has been a Research Assistant since 2014. His research interests include differential GNSS navigation, sensor fusion, and autonomous UAVs.

THOMAS WALTER was born in Osterburg, Germany, in 1983. He received the M.S. degree in electrical engineering from the University Bremen in 2011. From 2005 to 2011, he was a Student Assistant with the Center of Applied Space Technology and Microgravity, ZARM, Bremen. Since 2011, he has been a Research Assistant with the Department of Aerospace Information Technology, University of Würzburg. He was the Project Leader in VIDANA and VaMEx-LAOLa both funded by DLR. His research interests include highly reliable distributed systems and local position determination systems.

JULIAN ROTHE was born in Leipzig, Germany, in 1990. He received the B.S. degree in aerospace computer science and the M.S. degree in computer science from the University of Würzburg, Würzburg, in 2012 and 2016, respectively, where is currently pursuing the Ph.D. degree with the Department of Aerospace Information Technology. Since 2017, he has been a Research Assistant with the Department of Aerospace Information Technology, University of Würzburg. He leads the MIDRAS Project, which aims to develop an autonomous cooperative UAV system that is capable of catching micro drones in mid-air with a net.

SERGIO MONTENEGRO was born in Guatemala City, Guatemala, in 1959. He received the B.S. degree from the Universidad del Valle in 1982 and the M.S. degree in computer science and the Ph.D. degree from the Technical University of Berlin in 1985 and 1989, respectively. He was a Research Assistant in distributed computing with the Fraunhofer-Gesellschaft Institut, Berlin, from 1985 to 2007. From 2007 to 2010, he was the Leader of the Department of Central Avionic Systems, DLR, Bremen. Since 2010, he has been a Professor and the Chair of the Department of Aerospace Information Technology, University of Würzburg, Germany.